Direct Numerical Simulations of Three-dimensional Hypersonic Flow over a Flat Plate with Periodic Holes

Adriano Cerminara*, Ralf Deiterding† Neil D. Sandham ‡
Aerodynamics and Flight Mechanics Research Group
University of Southampton, Southampton, Hampshire, SO17 1BJ, United Kingdom

August 7, 2017

Abstract

A numerical study is presented which investigates, through direct numerical simulation (DNS) of the Navier-Stokes equations, the main characteristics of a three-dimensional (3D) hypersonic flow at Mach 6 over a flat plate with periodic pores in both the streamwise and spanwise directions. Some preliminary two-dimensional (2D) simulations have been run first, through which an initial validation of the numerical code, a grid convergence study, and a parametric study showing the sensitivity of the solution to different Reynolds numbers and wall temperatures have been performed. The method used to carry out the numerical simulations consists of a 6^{th}-order central differencing base scheme, in conjunction with a shock-capturing symmetric 6^{th}-order weighted-essentially-non-oscillatory (WENO) scheme, which provides higher numerical stability in the critical regions of strong gradients while minimising the numerical dissipation in smooth regions. The results show the capabilities of the code in carrying out high-resolution simulations with relatively low computational cost for the present configuration. The viscosity effects relative to a lower Reynolds number have been found to enhance fluid trapping and recirculation within the pores in the 2D case, however in the 3D case internal recirculation is enhanced at the higher Reynolds number via more influent 3D flow effects. Moreover, acoustic waves have been found to be radiated from the pore edges into the boundary layer, which are stronger at the lower Reynolds number. An increase of the radiated acoustic-field amplitude has been observed to be induced also by wall cooling. The three-dimensional characteristics of the flow nearby the pores are presented and discussed for two different Reynolds numbers.

*Research Fellow
†Associate Professor of Aerospace Engineering
‡Professor of Aerospace Engineering

1 Introduction

The aero-thermal design of hypersonic vehicles is crucial for the structural integrity of the vehicle and for the mission performances, due to the severe wall heating effects encountered at hypersonic speeds. The hypersonic flow environment is, in fact, characterised by large amounts of kinetic energy gradually dissipated within the boundary layer through viscous effects, and converted into thermal energy. This produces high temperature peaks inside the boundary layer at small normal distances from the wall, which provide, in turn, high temperature gradients at the wall. The aerodynamic heating due to the viscous effects inside the boundary layer is the main source of wall heating over most of the surface of slender bodies (e.g. cruise vehicles) flying at hypersonic speeds. For blunt reentry bodies (e.g. the Apollo-like capsules), instead, wall heating is primarly due to the kinetic energy converted into thermal energy downstream of the strong bow shock wave in front of the body, which increases the temperature inside the shock layer up to extremely high levels (consistent with the very high reentry velocities of a typical ballistic reentry), producing large wall heat-flux values at the stagnation point.

In order to reduce the wall heating effects, the hypersonic vehicles need an appropriate thermal protection system (TPS) capable of storing, or radiating/dissipating outwards, the high heat load, thus keeping the surface temperature of the internal structure within tolerable values. For lifting bodies (e.g. Space-Shuttle-like reentry vehicles, or cruise vehicles in general), reusable ceramic materials and carbon-carbon composite materials have been shown to be the most suitable materials for the TPS. In contrast, for ballistic reentry bodies, the higher heating loads encountered require the TPS to be formed of non-reusable polymeric ablative materials (usually consisting of a phenolic or epoxy resin matrix). Active cooling, which consists of injecting cold fluid into the boundary layer through localised holes (i.e. 'film cooling') or a porous coating (i.e. 'transpiration cooling'), can help meet the wall-temperature requirements for hypersonic vehicles by significantly reducing the wall temperature, avoiding the use of additional thermal protection layers.

In this context, laminar-turbulent transition plays a fundamental role in the aero-thermal design of hypersonic vehicles, due to a dramatic increase of the wall heat-transfer rates downstream of the transition point, which is caused by the turbulent mixing enhancing the mass and energy transport between different flow layers inside a turbulent boundary layer. As a consequence, an unpredicted transition to turbulence in regions of particularly high heat-transfer rates (e.g. the nose region) might result in a failure of the structure. In particular, the slender leading-edge geometries are the most exposed to this risk, as they are characterised by the highest heat-transfer rates, since the heat flux at the stagnation point (q_{sp}) is inversely proportional to the square root of the leading-edge nose radius (i.e. $q_{sp} \propto \sqrt{1/R}$ [1]).

In the presence of small environmental disturbances or small perturbations induced at the wall, transition to turbulence is caused by the growth of boundary-

layer unstable modes. In subsonic and low-supersonic (below Mach 4) boundary layers the first instability mode, corresponding to the Tollmien-Schlighting waves, is the dominant mode causing transition [2]. At higher Mach numbers, instead, namely at hypersonic speeds, other higher-frequency modes (belonging to the ultrasonic frequency band), so-called 'Mack' modes [3], are present and play a more relevant role in the transition process. Among these modes, the second mode, which usually appears for frequencies higher than 100 kHz, is known to be the dominant mode in 2D hypersonic boundary layers, as was observed in the experiment of Stetson *et al.* [4], in the theoretical studies of Fedorov and Khokhlov [5] and Fedorov [6], and in several other numerical works (e.g. [7, 8, 9, 10]).

Thus, wall cooling, from one side, and the ability to keep the boundary layer laminar up to longer distances, from the other side, play both a fundamental role in keeping efficiently the wall temperature below certain limit values, which in turn depend on the thermal properties of the TPS material. Laminar flow control (LFC) is the branch that focuses on the development of methods for the stabilisation of the boundary layer, by decreasing the amplification of the unstable modes, or even eliminating them. Stabilisation achieved through pressure gradient or shaping belong to the class of passive LFC techniques, while methods based on wall suction and heat transfer are known as active LFC techniques [2]. Wall cooling, in turn, can significantly affect transition, as it provides in general stabilisation or destabilisation effects depending on the cases. In particular, wall cooling has a strong stabilisation effect on the first instability mode, while destabilises the second mode. As the second mode is dominant at hypersonic Mach numbers, the direct beneficial effects of wall cooling on the wall temperature may be lost due to the simultaneous destabilisation of the second mode, which would move the transition point upstream.

However, several theoretical studies [2, 11, 12], have shown that passive porous coatings have an important stabilisation effect on the second instability mode, whose main implication is the delay of transition. Different experimental investigations, e.g. [2, 14, 13], have confirmed the stabilisation effects of the porous coatings, considering both regular and random microstructures, as well as linear and nonlinear stages of the boundary-layer disturbances. The work of Lukaschevich *et al.* [13], in particular, has shown the sensitivity of the second mode on the position of the porous coating along the wall, indicating that the second mode is stabilised if the coating is applied within the instability region of the mode, while is destabilised if the coating is located in its stable region, thus confirming qualitatively the results of the previous numerical work of Wang and Zhong [15]. The effects of the pore shape and size on the stabilisation performances has been investigated numerically by Wartemann *et al.* [16], showing an additional damping effect provided by an increase of the pore diameter, while the theoretical study of Wartemann *et al.* [17] has investigated the absorption characteristics of carbon fiber reinforced carbon ceramic (C/C), demonstrating a strong damping effect on the second mode. Finally, the work of Lukaschevich *et al.* [18] has shown the agreement between numerical and experimental results concerning the role of the absorptive porous coating thickness on the stabilisa-

tion of the second mode, revealing that there is an optimal thickness at which maximum stabilisation is reached, which then allows the design and manufacturing of relatively thin efficient coatings.

Hence, an effective wall cooling at hypersonic speeds can be achieved if the active cooling is associated to a porous coating capable of absorbing the ultrasonic unstable waves relative to the second instability mode. This clearly indicates that the transpiration cooling technique is well suitable for the hypersonic flow environments, and preferable to the film cooling technique, provided the porous material satisfies the required criteria for boundary-layer stabilisation. In this paper we present 2D and 3D direct numerical simulations investigating the main characteristics of a hypersonic laminar boundary layer at Mach 6 over a flat plate with periodic holes for different Reynolds numbers and wall temperature conditions. This work serves as an initial parametric and validation study for the future numerical investigation of the stabilisation properties with different microstructures, aimed at the design of efficiently stabilising transpiration cooling systems.

2 Numerical method

2.1 Governing equations

We consider numerical solutions of the three-dimensional Navier-Stokes equations for compressible flows, written in conservation form, under the assumption of a perfect gas. The set of non-dimensional conservation equations in Cartesian coordinates can be written as

$$\frac{\partial \mathbf{Q}}{\partial t} + \frac{\partial (\mathbf{F}_j)}{\partial x_j} = 0 \, .$$

In the equation above, $\mathbf{Q}$ is the vector of the conservative variables, while $\mathbf{F}_j$ is the vector of the fluxes in Cartesian coordinates. The components of the vectors of the system in conservative form are

$$\mathbf{Q} = \begin{bmatrix} \rho \\ \rho u \\ \rho v \\ \rho w \\ \rho E \end{bmatrix} ,$$

$$\mathbf{F}_j = \begin{bmatrix} \rho u_j \\ \rho u u_j + \delta_{1j} p - \frac{1}{Re}\tau_{1j} \\ \rho v u_j + \delta_{2j} p - \frac{1}{Re}\tau_{2j} \\ \rho w u_j + \delta_{3j} p - \frac{1}{Re}\tau_{3j} \\ \rho\left(E + \frac{p}{\rho}\right) u_j - \frac{1}{Re}\left(u\tau_{1j} + v\tau_{2j} + w\tau_{3j} + \frac{\mu}{(\gamma-1)PrM^2}\frac{\partial T}{\partial x_j}\right) \end{bmatrix} .$$

The terms ρ, ρu, ρv, ρw and ρE are the conservative variables of the system of equations, where ρ is the density, u, v and w are the velocity components respectively in the x-, y- and z-directions, and E is the total energy per unit mass. In the flux vectors, the terms p, T, τ_{ij}, and μ are respectively the pressure, the temperature, the components of the viscous stress tensor, and the dynamic viscosity of the flow. The non-dimensional quantities are obtained through normalisation of the dimensional variables with their freestream reference values: the velocity components are normalised with the freestream main velocity (U^*_∞), the density is normalised with the freestream density (ρ^*_∞), the viscosity is normalised with the freestream dynamic viscosity (μ^*_∞), the temperature is normalised with the freestream temperature (T^*_∞), the total energy is normalised with the square of the freestream mean velocity (U^{*2}_∞), while the pressure and viscous stresses are normalised with the term $\rho^*_\infty U^{*2}_\infty$, related to the freestream dynamic pressure. Note that the superscript (*) is used to denote dimensional values. The boundary-layer displacement thickness (δ^*) is chosen as the characteristic length to normalise the length scales, while the time scales are normalised with respect to the fluid dynamic characteristic time (δ^*/U^*_∞), based on the velocity of the undisturbed flow and on the characteristic length. The terms Re, Pr, M, and γ are respectively the Reynolds, Prandtl and Mach numbers, and the ratio of specific heats ($\gamma = c^*_p/c^*_v$), i.e. the dimensionless parameters of the flow. The Reynolds number is defined with respect to the boundary-layer displacement thickness of the similarity solution, as $Re = (\rho^*_\infty U^*_\infty \delta^*)/\mu^*_\infty$; the Prandtl number is set to 0.72 for air, and γ is equal to 1.4, as we are considering a perfect gas model. The dynamic viscosity is, in turn, expressed in terms of temperature by Sutherland's law

$$\mu = T^{3/2}\frac{1+C}{T+C} ,$$

where the constant C represents the ratio between the Sutherland's constant (set to 110.4 K) and the reference temperature in the freestream T^*_∞. The viscous stresses are defined in terms of the velocity derivatives, under the assumption of a Newtonian fluid, as

$$\tau_{ij} = \mu \left[\frac{\partial u_i}{\partial x_j} + \frac{\partial u_j}{\partial x_i} - \frac{2}{3}\delta_{ij} \frac{\partial u_k}{\partial x_k} \right] .$$

We also need a relation linking the total energy to the temperature, which in non-dimensional form can be expressed as

$$E = \frac{T}{\gamma(\gamma-1)M^2} + \frac{1}{2}\left(u^2 + v^2 + w^2\right) \ .$$

Finally, the system of equations is closed by the equation of state for a perfect gas

$$p = \frac{1}{\gamma M^2}\rho T \ .$$

2.2 Code features

The numerical simulations have been carried out using the code AMROC [19, 20] (Adaptive Mesh Refinement in Object-oriented C++), which uses a hybrid WENO-centred-difference (WENO-CD) scheme in conjunction with a structured adaptive mesh refinement (SAMR) approach. The implementation relative to the base central scheme is equipped with the option to be opportunely tuned (or optimised) for spectral resolution improvement, which denotes the scheme as WENO-tuned-centred-difference (WENO-TCD), as described by Hill and Pullin [21]. The shock-capturing filter, namely the WENO scheme, corresponds to the type of WENO-symmetric-order-optimised (WENO-SYMOO) scheme as shown by Martin *et al.* [22]. The schemes are integrated with a switching function that turns on/off the WENO method at discontinuities/smooth regions.

The base scheme (central scheme) has been proven to have a maximum formal order of accuracy of 6, corresponding to a 7 point stencil, with relative stencil coefficients as in Ziegler *et al.* [23]. It represents the most relevant part of the overall computational method, thus it determines the main performances for DNS. The order of accuracy can be properly specified, which changes the stencil, and can be also reduced (keeping constant the stencil) for optimisation of the bandwith resolution capabilities. For example, considering the 7-point stencil, if the optimisation option is specified, the corresponding scheme will be

a 4-th order accurate scheme with optimised bandwith properties [21], thus having a minimum dispersion error of the modified wavenumber, suitable for LES (Large-Eddy-Simulation) simulations. However, this is not advisable for DNS computations, where one wants to guarantee minimum truncation error, thus maximum formal order of accuracy. Hence, our reference base method for DNS can be considered the regular 6-th order central scheme (with which the version of the code can be defined as WENO-CD), through which the approximated fluxes at the cell interfaces ($\hat{f}_{i+\frac{1}{2}}$) are evaluated as

$$\hat{f}_{i+\frac{1}{2}} = \alpha(f_{i+3} + f_{i-2}) + \beta(f_{i+2} + f_{i-1}) + \gamma(f_i + f_{i+1}) \ ,$$

with $\alpha = 1/60$, $\beta = -2/15$, and $\gamma = 37/60$.

The shock capturing part of the code (WENO) is fundamental for problems with discontinuities, and can make the difference in the performances of the DNS tool in problems of compressible turbulence. The WENO method itself represents a robust shock-capturing scheme and historically one of the best compromises between added numerical dissipation and high-order accuracy. It is in general less dissipative than the TVD (total-variation-diminishing) scheme, which makes it suitable for high-resolution DNS applications. The currently implemented version of the WENO scheme is an improved higher-order version of the original WENO-JS scheme of Jiang and Shu [24]. In particular, the WENO-JS version used 3 upwinded-biased candidate stencils with $r = 3$ points, reaching a maximum formal order of accuracy of $2r-1 = 5$. While the improved version (described in Martin *et al.* [22]) applies two basic modifications to the WENO-JS version, namely i) another 3-point stencil is added which gives symmetrisation of the scheme, thus reducing the numerical dissipation (which leads to the definition of the scheme as WENO-SYM); ii) new optimal weights C_k (for the smooth regions) are provided, which guarantee maximum formal order of accuracy of 6 (i.e. $2r$). Thus, the new symmetric increased-order of accuracy WENO scheme is referred to as order-optimised WENO scheme, or WENO-SYMOO, which is the version considered in Ziegler *et al.* [23]. Considering, for simplicity, the one-dimensional advection equation,

$$\frac{\partial u}{\partial t} + \frac{\partial f(u)}{\partial x} = 0 \ ,$$

whose discretised form in space, in the finite-volume method approach, is

$$\hat{u}_{i,t} = -\frac{1}{\Delta x}(\hat{f}_{1+\frac{1}{2}} - \hat{f}_{i-\frac{1}{2}}) \ ,$$

where $\hat{u}_i$ is the approximation of the variable u at the cell center i, the subscript t indicates the time derivative, and Δx is the grid spacing, the splitted numerical flux at one side of the cell interface $i+\frac{1}{2}$, in the considered version of the WENO scheme, is approximated by [22]

$$\hat{f}^{+}_{i+\frac{1}{2}} = \sum_{k=0}^{r} \omega_k q^r_k \ .$$

In the above formula, k indicates the k-th candidate stencil among those chosen to approximate the numerical flux function, r is the total number of candidate stencils ($r = 3$ in our case), q_k^r is a r-th-order polynomial interpolation of the numerical flux on the k-th stencil (evaluated at the point $i + \frac{1}{2}$) expressed as

$$q_k^r = \sum_{l=0}^{r-1} d_{k,l}^r f(u_{i-r+k+l+1}) \ ,$$

and ω_k is the weight relative to the k-th polynomial approximation. The stencil coefficients $d_{k,l}^r$ for the symmetric WENO scheme are listed in [22]. The weights are defined as

$$\omega_k = \frac{\alpha_k}{\sum_{k=0}^{r-1} \alpha_k} \ ,$$

in which the function α_k takes the form

$$\alpha_k = \frac{C_k}{(\epsilon + IS_k)^p} \ ,$$

where ϵ and p are two constants. For the optimal weights, C_k, the values reported in [22] relative to the WENO-SYMOO formulation are used. The function IS_k is a smoothness indicator, which assumes high values over discontinuities and small values in smooth regions, and is given by

$$IS_k = \sum_{m=1}^{r-1} \left(\sum_{l=0}^{r-1} b_{k,m,l}^r f(u_{i-r+k+l+1}) \right)^2 \ .$$

In smooth regions all the candidate stencils are equally taken into account, with no difference deriving from the smoothness indicator, so each k-th stencil contributes to the flux approximation through its optimal weight C_k. The coefficients $b_{k,m,l}$ are given in [22].

The switching function to turn on/off the WENO filter is based on the approximate solution of the left and right states of a Riemann problem at each cell interface through Roe's averaged state, as described in [23], in order to detect locally the presence and orientation of strong shock or rarefaction waves. Then, in the points where such a strong wave is found, the WENO scheme is applied, which provides numerical stability. In order to select only strong waves, while neglecting the weak ones, the method applies a threshold value to Liu's entropy condition [23], which is used to recognise the type of waves associated to the characteristic speeds in the left and right states. In particular, the difference of the eigenvalues $u \pm a$ between the left and the right states needs to be higher than the imposed threeshold value (α_{Liu}/a) for a wave to be considered strong enough to require the WENO method. Moreover, to increase the efficiency of the switching function, namely to minimise the use of the more computationally expensive WENO scheme (compared to the base central scheme), another

threeshold value is applied on a function based on the pressure gradient between two adjacent points, defined as

$$\phi(\theta_i) = \frac{2\theta_i}{(1+\theta_i)^2} \ ,$$

and

$$\theta_i = \frac{|p_{i+1} - p_i|}{|p_{i+1} + p_i|} \ ,$$

through which the WENO method is allowed only in the high pressure gradient regions, where the function $\phi(\theta_i)$ is above the threeshold value.

Finally, the code works in conjunction with a structured adaptive mesh refinement (SAMR) algorithm [19], through which the uniform grid is dynamically refined with consecutive finer grid levels during the iteration cycles, following a patch-wise refinement strategy. This applies in some particular regions of the flow where numerical instabilities, related to low initial grid resolution, are detected by means of error indicators.

The code has been tested to 6-th order accuracy (for both CD and the WENO parts) for both the 2D and the 3D porous wall test cases, giving very good results (which will be shown later in this paper), thus showing to be suitable for DNS computations of the current problem.

3 Geometrical configuration

The simulations have been run for both a 2D and a 3D configuration. The 2D simulations serve for grid convergence study, code validation and an initial parametric study based on the effects of the Reynolds number and the wall temperature. The 3D case shows the capabilities of the code to carry out high-resolution DNS simulations over a porous coating, and provide initial important data for the main characteristics of the 3D flowfield in the pore region, which will be used as a reference for a future study on the laminar flow control and transpiration cooling performances of porous coatings with different pore structures. Figure 1 represents the geometrical configuration considered in the 2D simulations.

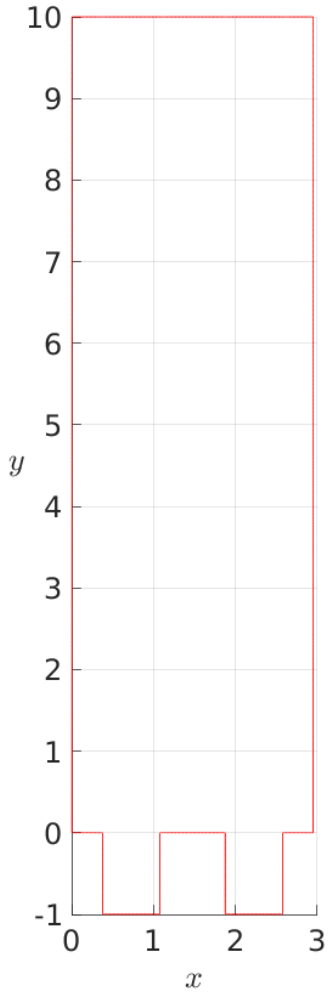

Figure 1: Computational domain geometry for the 2D simulations

As can be seen a very simple geometry has been chosen for the 2D test cases, consisting of 2 pores with regular shape in the x-direction. The length scales are dimensionless, normalised with the initial laminar boundary-layer displacement thickness of the present case, whose length assumes, then, the value of 1 in the nondimensional reference system (the corresponding dimensional value will be given in the section relative to the settings of the numerical simulations). Thus, the 2D computational domain is 3 times the initial boundary-layer displacement thickness, in the x-direction, and 11 times in the y-direction. The pores have a x-wise length of 0.75, and a depth of 1. The large extension of the domain in the y-direction is due to the need of allocating enough vertical space for the propagation of disturbance waves generated by the pores.

Figure 2 shows the domain considered in the 3D simulations.

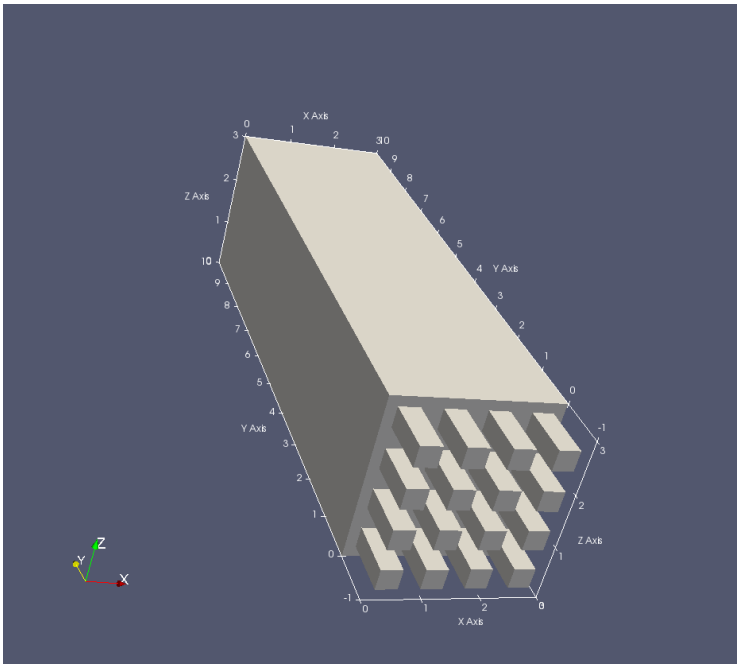

Figure 2: Computational domain geometry for the 2D simulations

The length of the 3D domain is 3 in both the x- and the z-directions, while the number of pores along each direction, compared to the 2D case, has been increased to 4, thus providing a 3D porous layer composed overall of 16 equally-spaced square-shaped pores. The pores have a length of 0.375 in both the x- and the z-directions. This configuration corresponds to the configuration analysed in the reference DNS study of De Tullio and Sandham [25].

4 Settings of the numerical simulations

Table 1 shows the freestream conditions (in dimensional quantities) relative to our numerical simulations. We consider 2 Reynods numbers, based on the boundary-layer displacement thickness, namely $Re = 6000$ and $Re = 20000$. The wall temperature is fixed to the adiabatic wall temperature for the present case, i.e. $T_w^* = T_{ad}^* = 7.027 T_\infty^* = 1522.4$ K. The reference length is the displacement thickness of the initial laminar boundary layer of the similarity solutions, through which the flowfield is initialised in our numerical simulations. Table

Table 1: Freestream conditions

Quantity	Value
M_∞	6
T^*_∞	216.65 K
$T^*_{0,\infty}$	1776.53 K
U^*_∞	1770.4 m/s
ρ^*_∞	1.534 kg/m^3
p^*_∞	9.54×10^4 Pa
ν^*_∞	9.55×10^{-6} m^2/s

Table 2: Dimensional values of the reference boundary-layer displacement thickness (δ^*) and the pores size (l^*_p)

Re	δ^* (mm)	2D case, l^*_p (mm)	3D case, l^*_p (mm)
6000	0.0323	0.024	0.012
20000	0.107	0.08	0.04

2 shows the dimensional values of the reference boundary-layer displacement thickness for each Reynolds number, as well as the corresponding values of the pores size, namely the length of each square-shaped pore in both the streamwise and spanwise directions (denoted by l^*_p), in the 2D and the 3D simulations.

On the wall sides, the usual no-slip boundary condition and an isothermal boundary condition (with wall temperature equal to the adiabatic value, T_{ad}, as explained above) are applied. An outflow boundary condition is applied on the top edge of the computational domain, while periodic boundary conditions are assumed on the sides in both the x-(streamwise) and z-(spanwise) directions. This means that the boundary layer is allowed to grow with time, as the considered configuration corresponds to following the streamwise evolution of the boundary layer along an infinite flat plate, within a window (i.e. the computational domain) moving along the flat plate in the x-direction (as U_∞ is in the x-direction). Thus, in the 3D simulations the initial boundary layer is 2D, as the flow enters the domain from the left hand side ($x = 0$) with a velocity directed along the x-axis, then it forms 3D flow features, during the iteration cycles, due to the presence of the pores. The periodic boundary conditions in the spanwise direction guarantee the periodicity of the perturbations of the mean 2D flow in the z direction, thus simulating an infinitely long porous sheet in the spanwise direction.

The effect of the wall cooling on the flowfield characteristics have been studied for the 2D configuration. In particular, two lower values of the wall temperature, with respect to the initial adiabatic wall temperature, have been considered, namely $T_w = 0.8T_{ad}$ and $T_w = 0.5T_{ad}$. The results of the 2D and the 3D numerical simulations will be shown in the next sections of the present paper.

5 Code validation and performances

5.1 2D test cases - Comparison between AMROC and SBLI

Preliminary 2D simulations have been carried out, for the Reynolds number $Re = 6000$, to validate the code and test its performances in comparison to SBLI, a DNS code developed over a number of years at the University of Southampton, which has been extensively tested and validated in the past showing excellent results (e.g. [26]).

Figures 3 and 4 show solutions of the pressure field (at the time dimensionless $t = 10$) obtained with the codes AMROC and SBLI respectively, with mesh resolution 64×356 (in the x and y directions) out of the pores. As can be seen, very similar results are obtained with the 2 codes, which demonstrates the accuracy capabilities of our considered code (AMROC). Also, the figures show that acoustic waves are formed at the pore edges, which propagate outwards influencing the flow outside of the boundary layer. Figure 5 shows a direct comparison between AMROC and SBLI for the density solution along x at $y = 1$. The result confirms the good agreement between the two different codes in accurately resolving the acoustic signal produced by the pores.

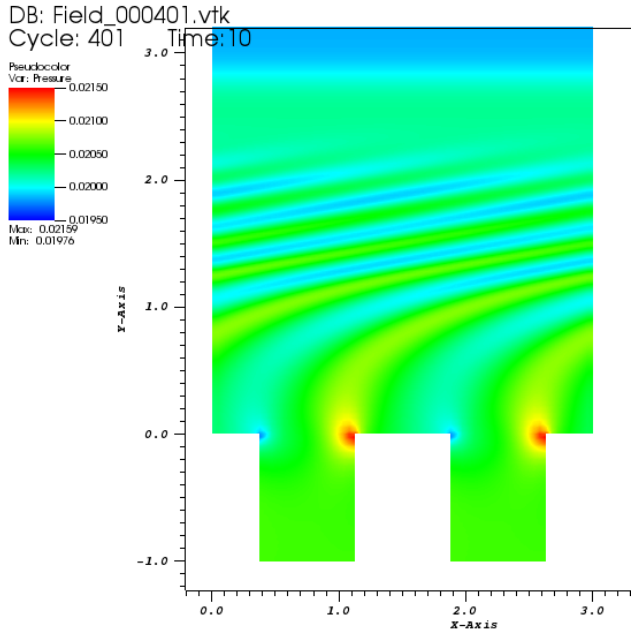

Figure 3: Pressure field at the time $t = 10$, with AMROC. 2D case

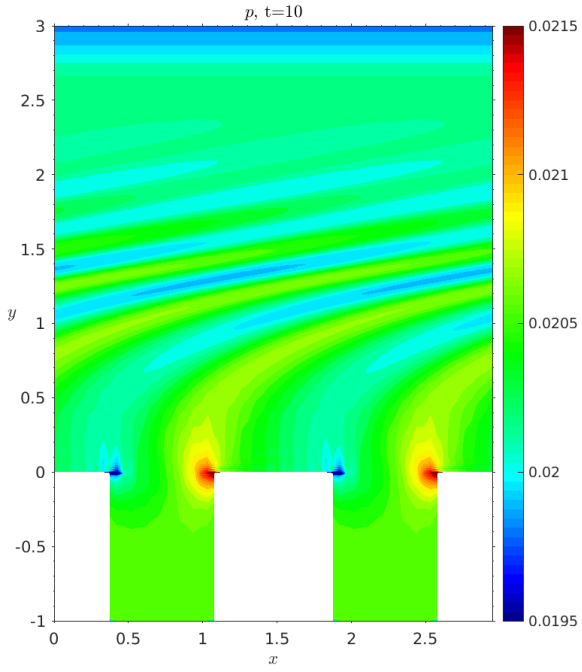

Figure 4: Pressure field at the dimensionless time $t = 10$, with SBLI. 2D case

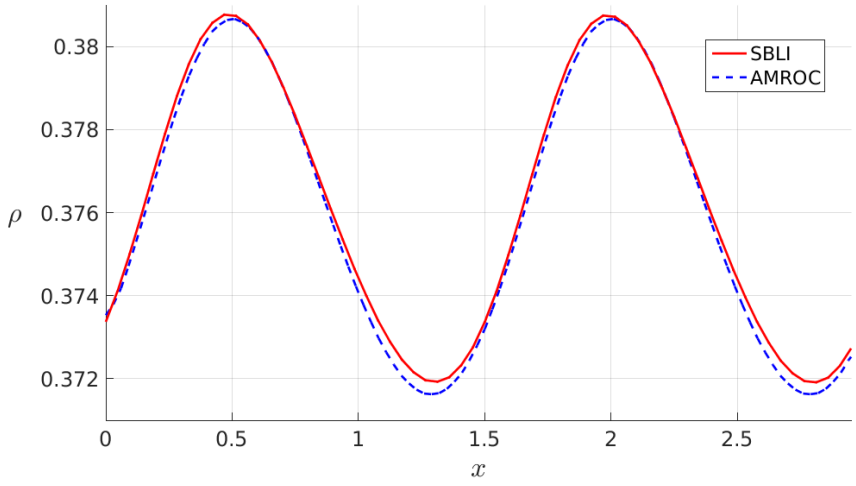

Figure 5: Comparison between AMROC and SBLI for the density trend along x at $y = 1$. Time $t = 10$.

Figures 6 and 7 show the cell flagging applied by the code to recognise the cells that are experiencing high gradients, which thus require switching from the central scheme to the WENO scheme for numerical stability. In the blue (smoother) regions of the flow the flag is zero, meaning that WENO is still turned off, while in the other flagged regions WENO is turned on. As said in Section 2.2 the switch is performed by means of two thresholds (for α_{Liu}/a and $\phi(\theta_i)$) opportunely imposed for each simulation. In particular, in figure 6 the threesholds correspond to the values of 0.02 and 0.002 respectively for α_{Liu}/a and $\phi(\theta_i)$, while the corresponding values in figure 7 are 0.05 and 0.005. So, as can be seen, higher theeshold values limit the WENO method in restricted regions of the flow characterised by higher gradients. In figure 6, in fact, WENO is allowed to work along the acoustic waves formed at the pore edges, which propagate upwards downstream, as is evident from the shape of the red zones (in figure 6) and as was seen in figure 3. In figure 7, in contrast, WENO is active only at the pore edges, which are the regions of the flow where the strongest pressure gradients take place, as is evident in figure 3. The simulation relative to figure 7 is then more efficient, as it guarantees numerical stability of the method where is strictly neccessary, thus reducing the computational cost (which increases when using the WENO method).

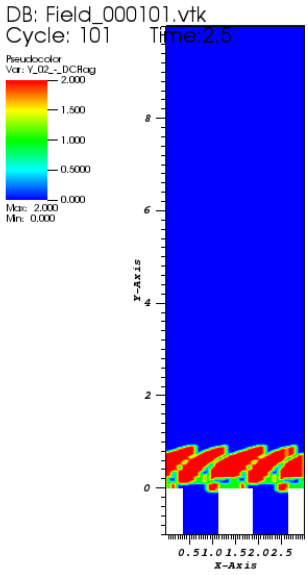

Figure 6: Flagging for CD-WENO switching, with the switching threesholds for α_{Liu}/a and $\phi(\theta_i)$ fixed to 0.02 and 0.002 respectively. The blue region (flag=0) is solved by the CD scheme only, while WENO is turned on elsewhere. Time $t = 2.5$

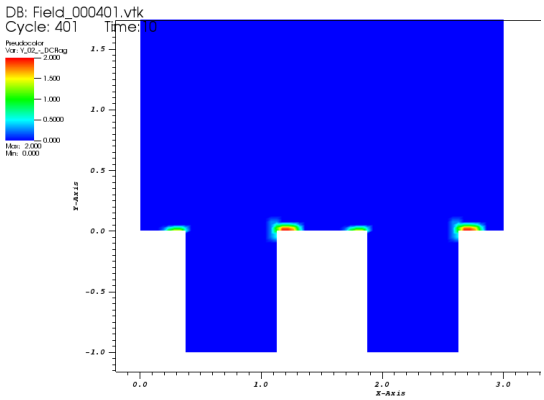

Figure 7: Flagging for CD-WENO switching, with the switching threesholds for α_{Liu}/a and $\phi(\theta_i)$ fixed to 0.05 and 0.005 respectively. The blue region (flag=0) is solved by the CD scheme only, while WENO is turned on elsewhere. Time $t = 10$

Table 3 shows the comparison between the performances of SBLI and AMROC in terms of execution time ($Time$), applied to the 2D porous wall test case. The effect of the method order on the computational cost is investigated as well. The grid size ($N_x \times N_y =$) is the same for the two codes. All the simulations have been run with 5 processors, and up to 5×10^3 time steps, with a fixed time step of $dt = 2 \times 10^{-3}$, corresponding to the simulation time $t = 10$. How can be seen, the 4^{th}-order WENO-CD scheme is the best high-order solution with an execution time lower by the 24 % with respect to SBLI, which, in turn, uses a 4^{th}-order central differencing scheme in conjunction with a 2^{th}-order Harten-Yee TVD shock-capturing filter. The low-order (2^{nd}) WENO-CD solution provides a further reduction of the execution time, of about the 9 % compared to the 4^{th}-order WENO-CD. The full WENO scheme provides, in contrast, a dramatic increase of the execution time. However, in this case, reducing the order from the 4^{th} to the 2^{nd} order provides a significant run-time reduction (about the 25 % lower compared to the 4^{th}-order WENO). This proves that the hybrid WENO-CD scheme is more computationally efficient than the method used by SBLI and the pure WENO method.

Table 3: Performances AMROC vs SBLI, 2D test case

Code	Method	Order	$N_x \times N_y$	dt	$Time(s)$	$\frac{\Delta Time}{Time^{SBLI}}$
SBLI	TVD-CD	4^{th}	64×487	2×10^{-3}	155.05	–
AMROC	WENO-CD	4^{th}	64×487	2×10^{-3}	117.77	-24%
AMROC	WENO-CD	2^{nd}	64×487	2×10^{-3}	106.83	-31%
AMROC	WENO	4^{th}	64×487	2×10^{-3}	839.51	$+441\%$
AMROC	WENO	2^{nd}	64×487	2×10^{-3}	626.24	$+304\%$

5.2 2D test cases - Grid resolution study

A grid resolution study has been carried out for the case at $Re = 6000$, based on the trend of the density along the streamwise direction at $y = 1$ (figure 9) and the pressure along the wall-normal direction at $x = 1.5$ (figure 9).

Six different grid resolution levels (for the base grid level in the SAMR framework) have been analysed, which allowed to investigate the effect of the grid refinement in the x- and y-directions (both simultaneously and separately), namely: 32×440, 64×440, 128×440, 64×660, 128×660, 128×880 (indicating the number of cells in the x- and y-directions respectively).

Both figures show a very good grid convergence within the considered grid resolutions. In particular, the solution for the oscillation peaks in figure 9 is shown to be more sensible to the grid resolution in the y-direction (when shifting from 440 to 660 cells), compared to the refinement in the x-direction. Here, the finest grid levels (128×660 and 128×880) are overlaid on the level 64×660 (dotted green line), which can be considered as the level where grid convergence is reached. The solution for the 64×440 base grid with 3 maximum grid levels for the adaptive mesh refinement is also shown for comparison, whose result appears to be in the middle between the grid levels with coarser (440 cells) and finer ($>$ 440 cells) y-resolution. Figure 9 shows excellent results of the grid resolution study for the pressure solution inside the boundary layer, which proves that at the considered (relatively cheap) grid resolution, e.g. 64×440, without the need for adding dynamically more refinement levels (through the SAMR methodology), we already manage to resolve very well the boundary layer for the present configuration.

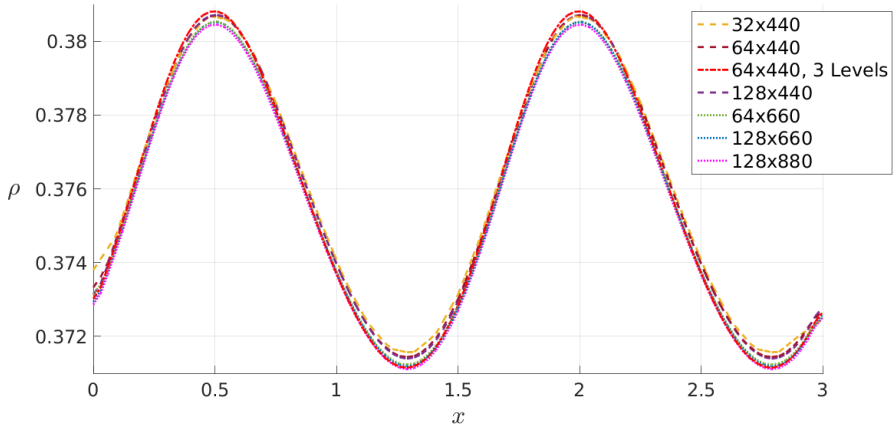

Figure 8: Grid resolution study for the density along x at $y = 1$, $Re = 6000$

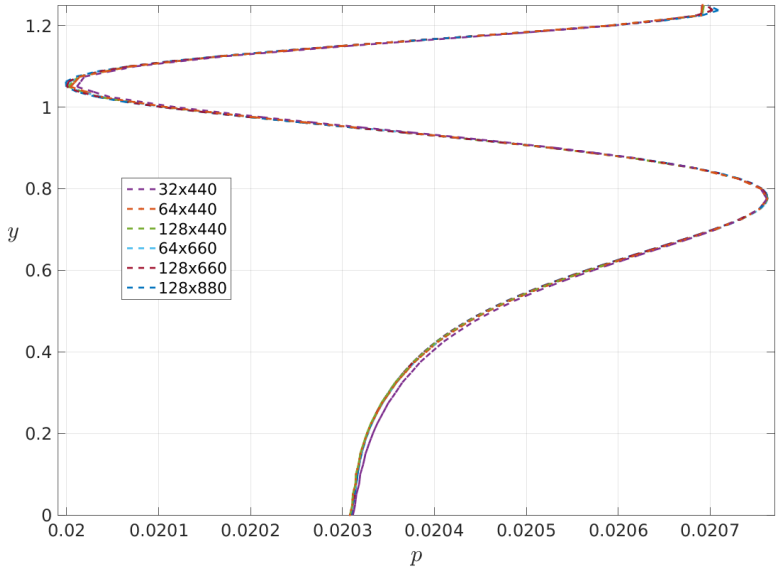

Figure 9: Grid resolution study for the pressure along y at $x = 1.5$, $Re = 6000$

Finally, a grid convergence study has been carried out also for the higher Reynolds number case ($Re = 20000$), based on the trend of the density along the streamwise direction at $y = 1$ (figure 10). In this case, it is evident that the effect of the y-resolution on the solution accuracy is more significant compared to the lower Reynolds number case. Grid convergence is reached within 660 and 880 cells in the y-direction, with a small effect of the resolution in the x-direction.

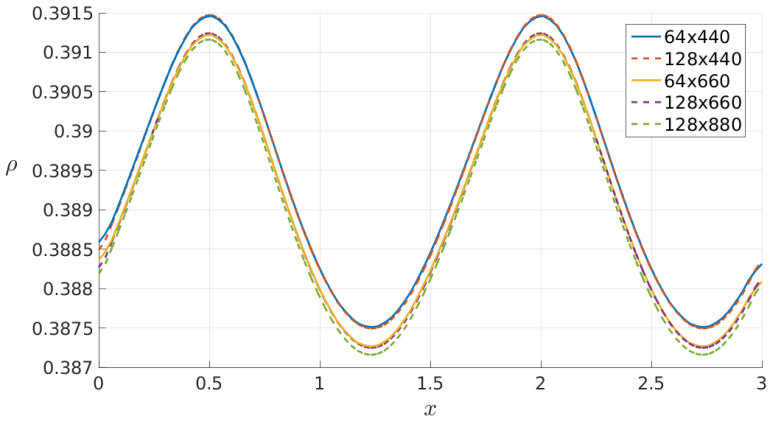

Figure 10: Grid resolution study for the density along x at $y = 1$, $Re = 20000$

6 Results

6.1 Initialisation

To show an example of the initialisation field, the initial density field of the similarity-solution laminar boundary-layer is plotted in figure 11. In particular, the initialisation inside the pores is made by imposing the physical quantities at each point inside the pores equal to their value at the wall on the flat plate surface.

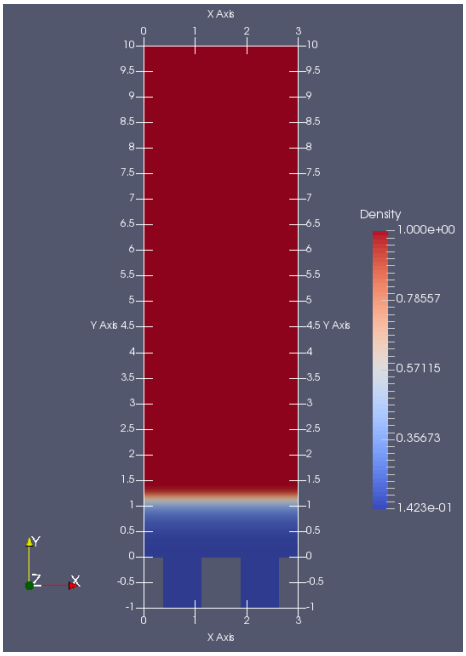

Figure 11: Density field of the initial laminar boundary-layer of the similarity solutions ($t = 0$). $Re = 6000$

6.2 2D results - Effect of Reynolds number

A preliminary parameter study has been performed for the 2D configuration on the sensitivity to the Reynolds number and the wall temperature. The effect of the Reynolds number on the solution for the pressure, temperature and vertical velocity fields is shown in figures 12, 13 and 14 respectively. As can be seen in figure 12, the lower Reynolds number is seen to induce higher pressure levels

inside the pores and in the boundary layer, with the effect of generating stronger acoustic disturbances at the boundary layer edge.

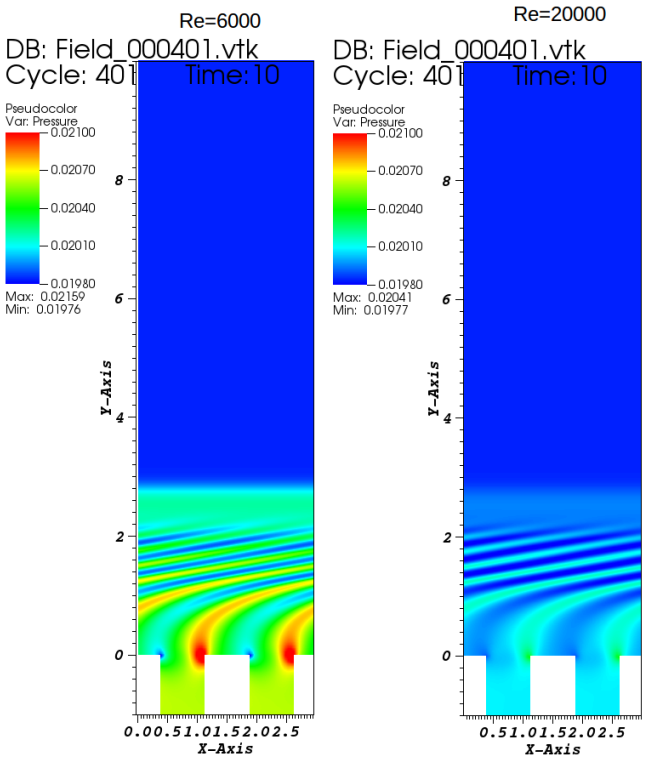

Figure 12: Reynolds number effect on the pressure field, for $Re = 6000$ (left) and $Re = 20000$ (right). Time $t = 10$

Consistent with the higher pressure levels, figure 13 shows that the flow indide the pores, dominated by the fluid viscosity, is characterised by higher temperature levels at the lower Reynolds number, with evident important consequences for the heat flux at the walls. It should be mentioned, however, that the boundary layer is laminar in the considered case (2D). The effect of a turbulent boundary layer at high Reynolds numbers on the wall heat flux will need to be investigated (in 3D applications).

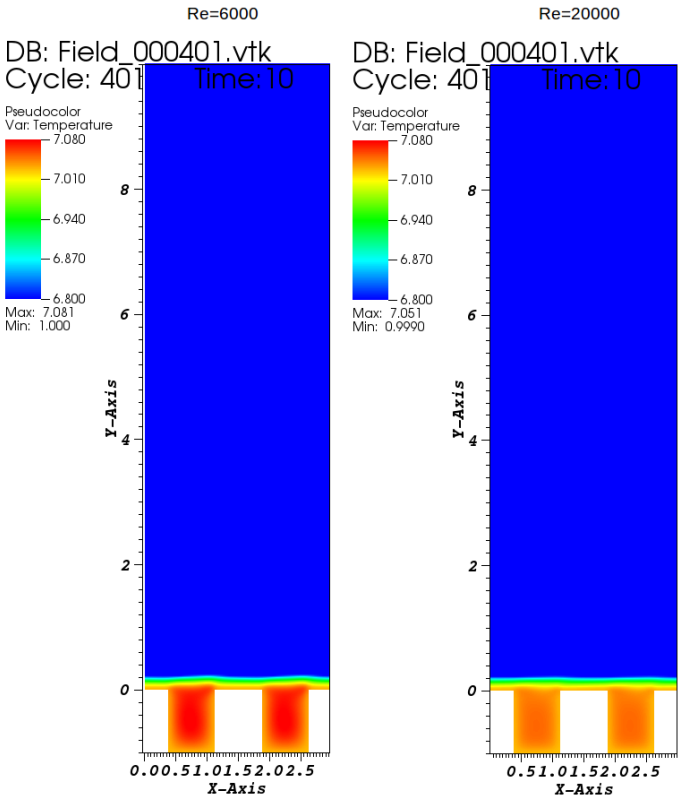

Figure 13: Reynolds number effect on the temperature field, for $Re = 6000$ (left) and $Re = 20000$ (right). Time $t = 10$. Note that the temperature layer looks very thin as an effect of the colour scale, that was set in such a way to highlight the differences inside the pores

Finally, figure 14 shows that higher absolute values of the vertical velocity are reached inside the pores for the lower Reynolds number case, compared to the higher Re. This is due to the higher effects of viscosity (dominating, as said above, the flow within the pores), which traps fluid from the boundary layer inside the pores, generating a more pronounced shear layer. At the higher Reynolds number, in contrast, the inertial effects along the streamwise direction are higher, and less recycling of fluid is induced inside the pores.

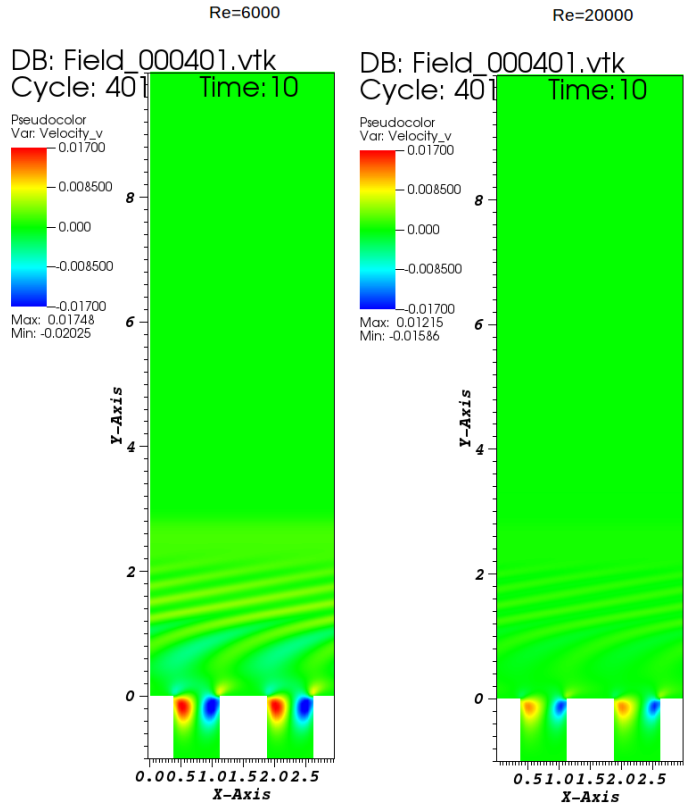

Figure 14: Reynolds number effect on the vertical velocity field, for $Re = 6000$ (left) and $Re = 20000$ (right). Time $t = 10$

6.3 2D results - Effect of wall cooling

The wall cooling effect is analysed (at $Re = 20000$) by comparing results for the temperature and pressure fields between the reference case with wall temperature equal to the adiabatic wall temperature ($T_{ad} = 7.027T_\infty$) and other two cooled wall cases, with wall temperature decreased by 20% and 50% of the initial adiabatic value, namely $T_w = 0.8T_{ad}$ and $T_w = 0.5T_{ad}$ respectively. Figures 15, 16 and 17 show the temperatue fields for the wall conditions $T_w = T_{ad}$, $T_w = 0.8T_{ad}$ and $T_w = 0.5T_{ad}$ respectively, while figures 18, 19 and 20 show the corresponding result for the pressure field, at the simulation time $t = 50$. As can be seen, the wall cooling produces an overall decrease of the temperature inside the boundary layer, which results in a lower boundary-layer thickness at the lower wall temperatures. This effect is related to the increase in density

inside the boundary layer as a result of the cooling.

Another remarkable effect of wall cooling on the temperature field is the gradual increase (with decreasing wall temperature) of the temperature inhomogeneity within the pores. In fact, while in the case of adiabatic wall temperature the temperature field appears more uniform, with a maximum temperature very close to the value at the wall ($T_w = 7.027$), as is shown more clearly in figure 13 (relatively to the case at $Re = 20000$), in the colder wall cases, in contrast, there is a higher difference between the maximum temperature region reached inside the pores and the wall temperature, namely a higher temperature gradient (which is larger the lower is the wall temperature). The high temperature region inside the pores, in the cooled wall cases, assumes an irregular shape (in contrast with the more symmetric shape assumed in the adiabatic wall temperature case, as seen in figure 13), which adapt to the high temperature values reached inside the boundary layer near the plate surface (over the pores) through the right pore corner, namely the highest pressure zone. The internal (i.e. inside the pore) flow nearby the left pore corner (where the expansion is located) is, in contrast, characterised by lower temperature values, which causes the asymmetry of the high temperature zone inside the pores. As this effect is more pronounced at the colder wall cases, it can have important implications on the heat-flux and the temperature distribution inside the coating material.

Moreover, looking carefully at figures 15 and 17, it is evident that wall cooling, due to the above described asymmetric effect on the internal high temperature region, produces a distortion of the boundary layer profile, in which the boundary layer is slightly thicker in correspondence of the axis of the high temperature region inside the pores. In general this can have a relevant effect on the stability properties of the boundary layer.

Figures 18, 19 and 20 show the effect of wall cooling on the pressure field, and in particular on the generated acoustic waves. It is evident that a decrease of the wall temperature produces a further decrease of the pressure in the low-pressure zones, namely in the zones corresponding to the negative peaks of the acoustic waves, which come from the left corner of the pores. This effect clearly is due to a pronounced low-pressure region generated inside the pores (as seen in figure 20) from the stronger expansion located at the left corner. At the same time, also the compression at the right corner becomes stronger (still with reference to figure 20), and produces higher pressure waves. Hence, the overall effect of a pronounced wall cooling over a porous surface consists in generating much stronger acoustic waves propagating outwards in the boundary layer and in the external field.

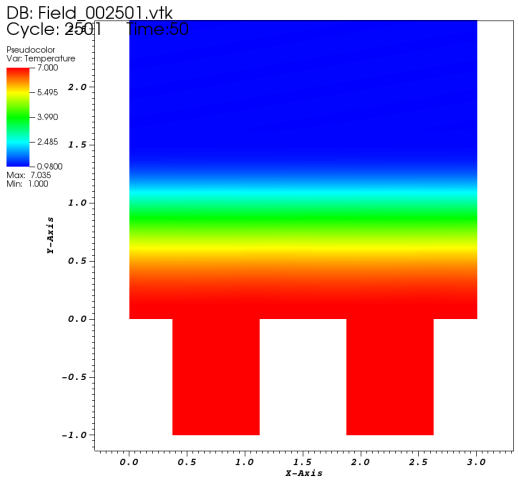

Figure 15: Temperature field for the wall temperature equal to the adiabatic value $T_w = T_{ad}$. Time $t = 50$, $Re = 20000$. Temperature colour bar range from 0.98 to 7

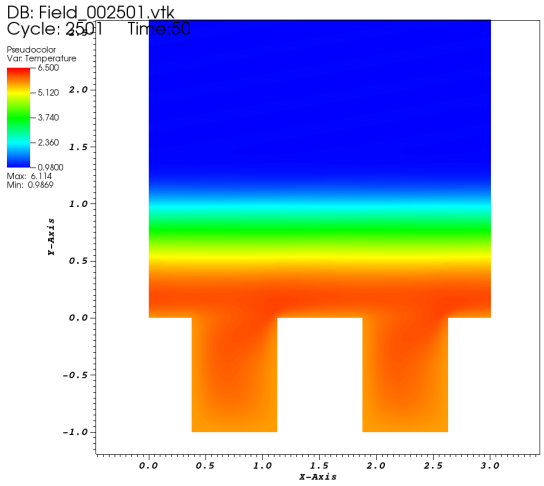

Figure 16: Temperature field for a cooled wall, with temperature equal to $T_w = 0.8T_{ad}$. Time $t = 50$, $Re = 20000$. Temperature colour bar range from 0.98 to 6.5

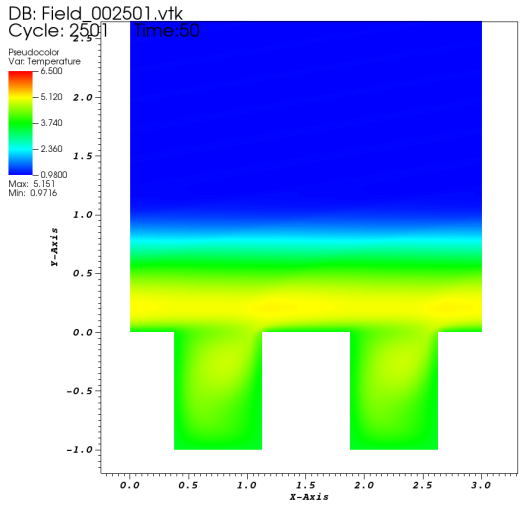

Figure 17: Temperature field for a cooled wall, with temperature equal to $T_w = 0.5T_{ad}$. Time $t = 50$, $Re = 20000$. Temperature colour bar range from 0.98 to 6.5

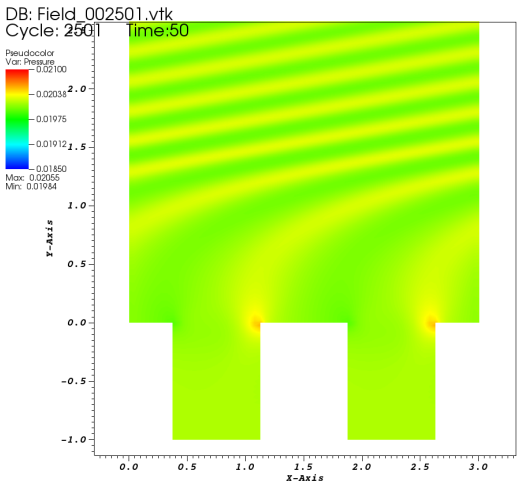

Figure 18: Pressure field for the wall temperature equal to the adiabatic value $T_w = T_{ad}$. Time $t = 50$, $Re = 20000$. Pressure colour bar range from 0.0185 to 0.021

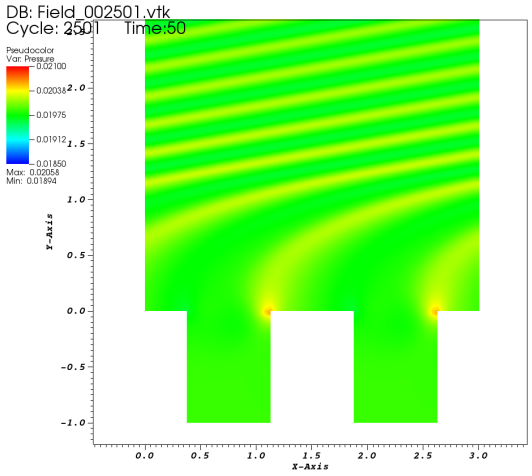

Figure 19: Pressure field for a cooled wall, with temperature equal to $T_w = 0.8T_{ad}$. Time $t = 50$, $Re = 20000$. Pressure colour bar range from 0.0185 to 0.021

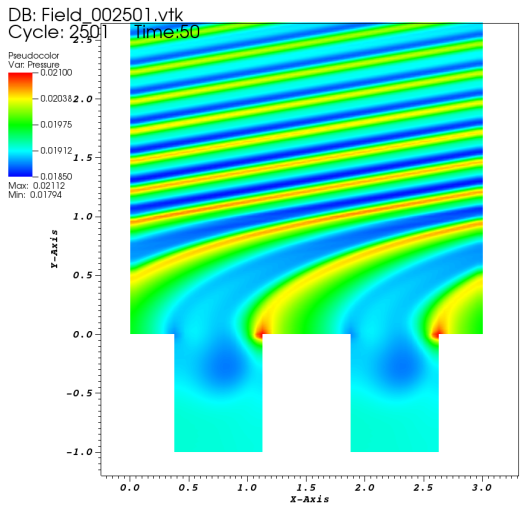

Figure 20: Pressure field for a cooled wall, with temperature equal to $T_w = 0.5T_{ad}$. Time $t = 50$, $Re = 20000$. Pressure colour bar range from 0.0185 to 0.021

6.4 3D results

High-resolution DNS simulations have been run for the 3D configuration with a mesh size $128 \times 660 \times 128$, using the 6^{th}-order WENO-CD method, in parallel over 96 cores, for both the Reynolds numbers ($Re = 6000$ and $Re = 20000$). The results of these simulations prove the high-resolution DNS capabilities of our considered code for the present case, apart from showing interesting highly-resolved 3D flow features of a hypersonic flow over a porous coating.

Figures 21 and 22 show examples of the 3D view of the pressure and vertical velocity fields, which give a first impression of the analysis performed for the present 3D configuration.

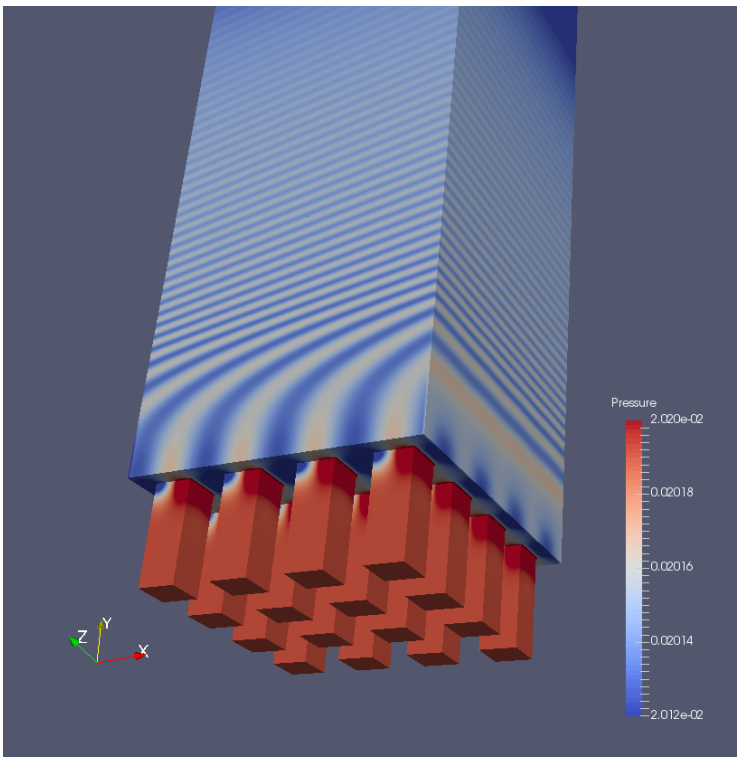

Figure 21: 3D view of the pressure field. Time $t = 50$, $Re = 20000$

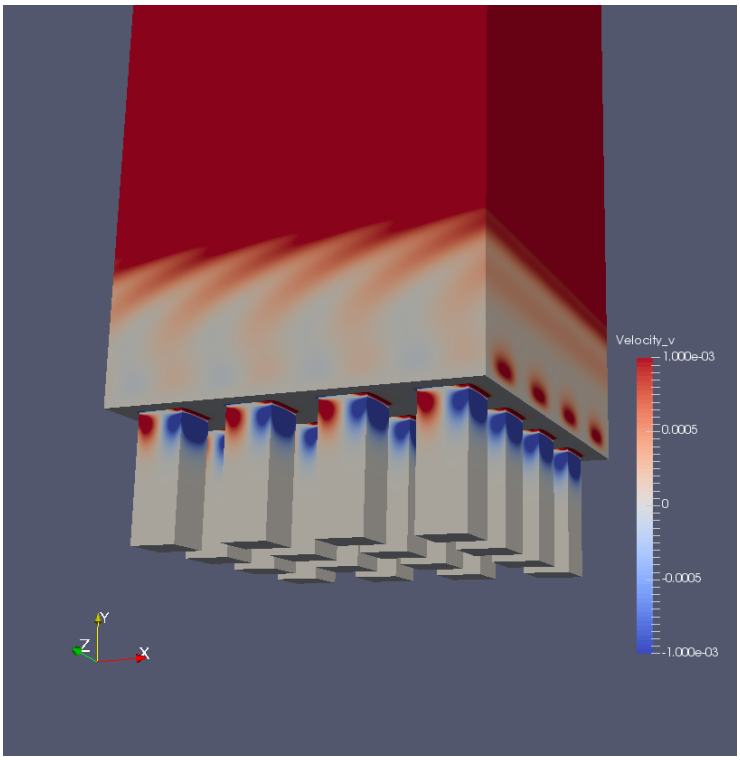

Figure 22: 3D view of the vertical velocity field. Time $t = 50$, $Re = 20000$

Figure 23 shows a comparison of the pressure field on a xy-slice at $z = 1.85$ between the two different Reynolds numbers. As can be seen, the lower Reynolds number case is characterised by stronger pressure disturbances radiated in the freestream by the pore edges. Moreover, it can be observed that, while at the higher Reynolds number the pressure level inside the pores seems much more comparable with that of the high pressure waves released in the freestream (compared to the lower Reynolds case), in the lower Reynolds number case the pressure level inside the pores is much higher than the level of the radiated waves. Hence, these results indicate that at lower Reynolds numbers the pores are characterised by higher values of the internal pressure.

Figure 24 shows the comparison of the pressure fields on a zy-slice at $x = 1.85$ for the two cases. Here, the colour range has been restricted to a smaller band in order to better notice the differences between inside and outside the pores for both cases. We observe again higher pressure waves travelling outside the boundary layer and, in general, a higher pressure amplitude in the pore region for the case at $Re = 6000$. It is possible also to notice (e.g. for the higher Reynolds number case) that the pressure field inside the pores is not uniform, but there is a slight variation of the pressure in the vertical direction, with the maximum values assumed in the first half of the pore depth (starting from

$y = 0$). Moreover, the modulation of the pressure field in the spanwise direction can be observed, which is remarkable in the immediate out-of-pore region, as a result of the 3D porosity of the wall.

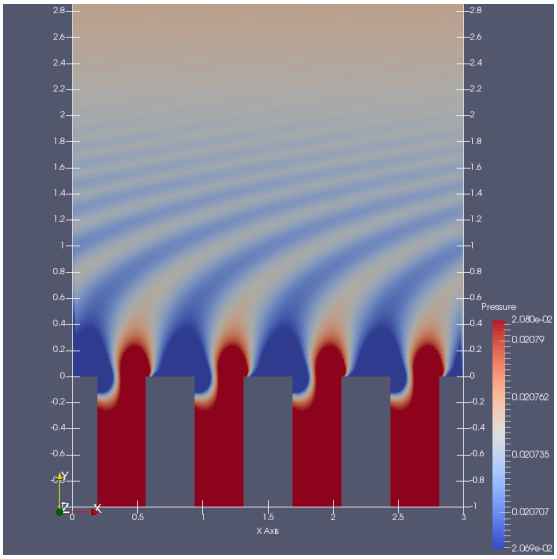

(a) $Re = 6000$

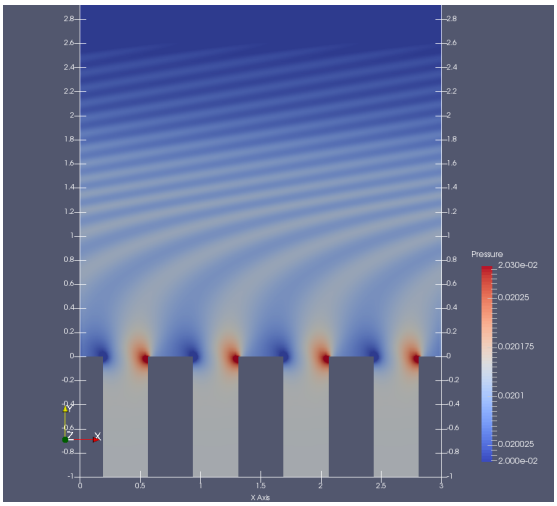

(b) $Re = 20000$

Figure 23: Pressure field on xy-slice at $z = 1.85$ inside the domain at $Re = 6000$ (a) and $Re = 20000$ (b)

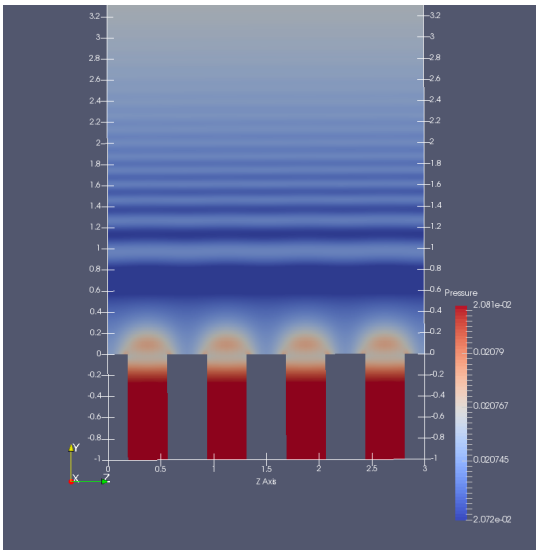

(a) $Re = 6000$

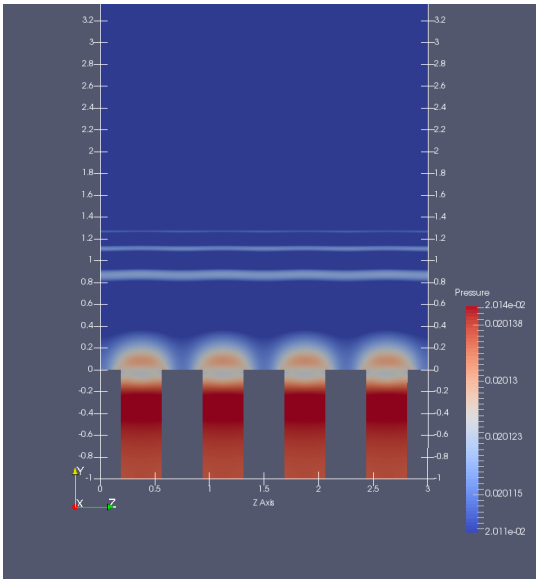

(b) $Re = 20000$

Figure 24: Pressure field on zy-slice at $x = 1.85$ inside the domain at $Re = 6000$ (a) and $Re = 20000$ (b)

A further analysis of the rms (root-mean-square) levels of the pressure disturbances outside the boundary layer (conducted at the height $y = 1.5$) has shown rms levels of p'_∞/p_∞ (i.e. the pressure fluctuations normalised with the

freestream pressure of the initial unperturbed flow) of 0.045 and 0.0154 for the lower and the higher Reynolds numbers respectively. Thus, at the lower Reynolds number, the pressure waves radiated by the porous wall are approximately 3 times stronger than the waves radiated in the higher Reynolds number case.

The vertical velocity field is analysed both in a xy-plane at the spanwise position $z = 1.85$ (in figure 25) and in a xz-plane at the vertical position $y = 0$ (in figure 26), namely at the surface plane. The former figure shows that higher absolute values of the inwards and the outwards velocity are reached immediately out of the pores at the lower Reynolds number. Also, higher positive values of the vertical velocity are observed outside of the boundary layer for the lower Reynolds number case, which is consistent with the presence of higher-amplitude radiated acoustic waves.

In figure 26 the three-dimensionality of the inwards and outwards flow on the pore surface is observed. Higher absolute values are seen for the lower Reynolds number case, consistent with the above discussion. However, another relevant difference is observed, namely, while the maximum absolute values of the vertical velocity are localised at the pore left and right sides (for the inwards and the outwards velocity respectively) at the lower Reynolds number case (which makes the flow at the pore intake more two-dimensional), at the higher Reynolds number, in contrast, the maximum of the inwards (blue coloured) velocity is detached from the left side, and localised in a three-dimensional region between the pore centre and the right side. This effect makes the region of the outwards flow flatter compared to the higher Reynolds number case, and produces a small zone of zero or slightly positive velocity (close-to-white region) nearby the left side. This suggests that at the higher Reynolds numbers the boundary-layer flow is trapped into the pores with a certain delay compared to the lower Reynolds numbers, which appears to produce a higher recirculation in the immediate inside-the-pore region, as seen from the higher absolute values shown in figure 25 below the upper pore surface for the higher Reynolds number case. This seems to be in contrast with what previously seen for the 2D simulations (with reference to figure 14), which showed higher recirculation inside the pores for the viscosity effect associated to the lowere Reynolds number. However, in this case, the 3D effects are responsible for this different behaviour at the higher Reynolds number, which then indicates that a higher Reynolds number flow is more sensitive to the 3D effects.

The last statement can be proven by observing the result for the spanwise velocity field at $y = 0$, in figure 27. Here, it can be seen that higher absolute values of the upwards and downwards (namely towards the higher and the lower z values respectively) spanwise velocity are reached respectively at the top-right and bottom-right corners of the pores for the higher Reynolds number case, which then demonstrates the presence of stronger 3D flow effects at a higher Reynolds number.

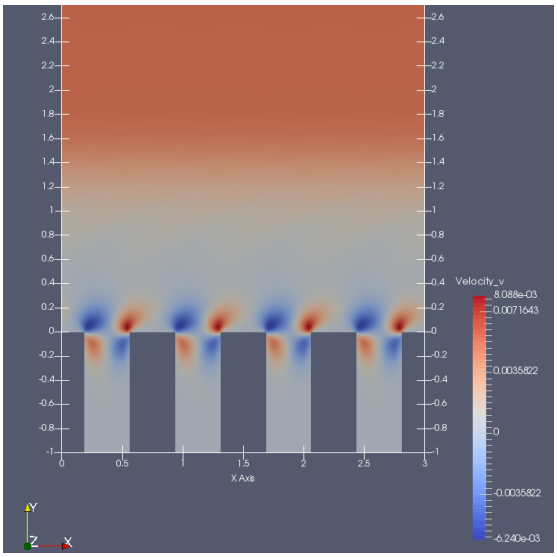

(a) $Re = 6000$

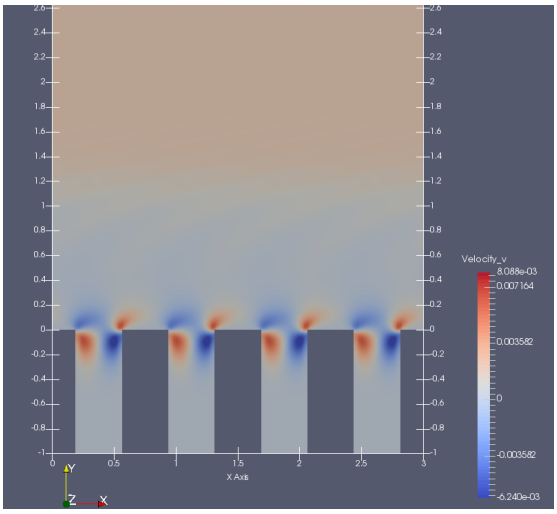

(b) $Re = 20000$

Figure 25: Vertical velocity field on xy-slice at $z = 1.85$ inside the domain at $Re = 6000$ (a) and $Re = 20000$ (b)

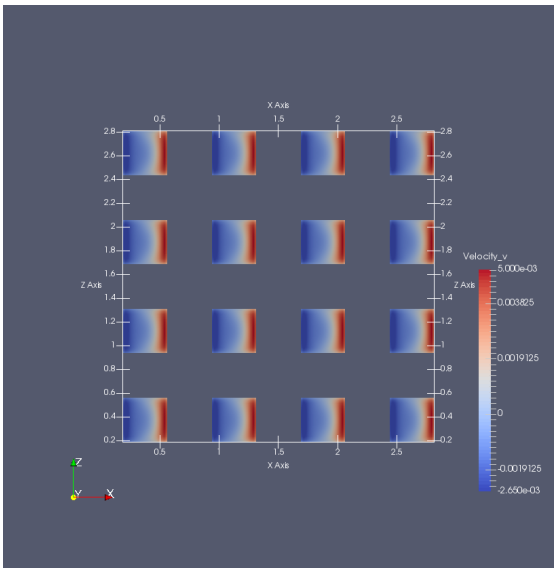

(a) $Re = 6000$

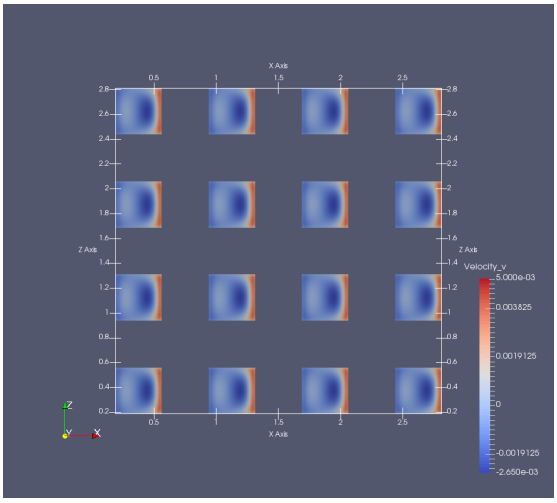

(b) $Re = 20000$

Figure 26: Vertical velocity field on xz-slice at $y = 0$ inside the domain at $Re = 6000$ (a) and $Re = 20000$ (b)

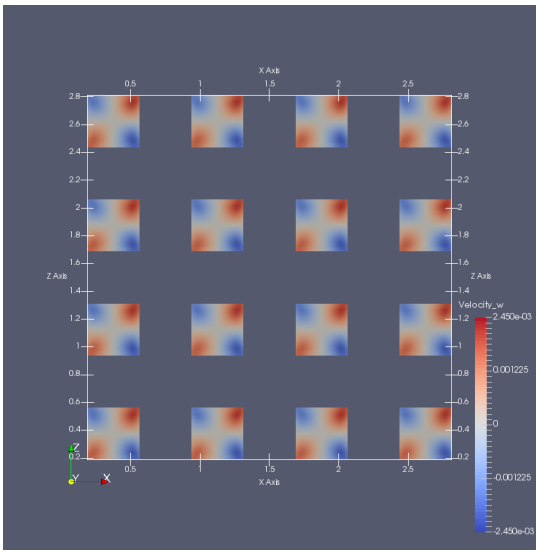

(a) $Re = 6000$

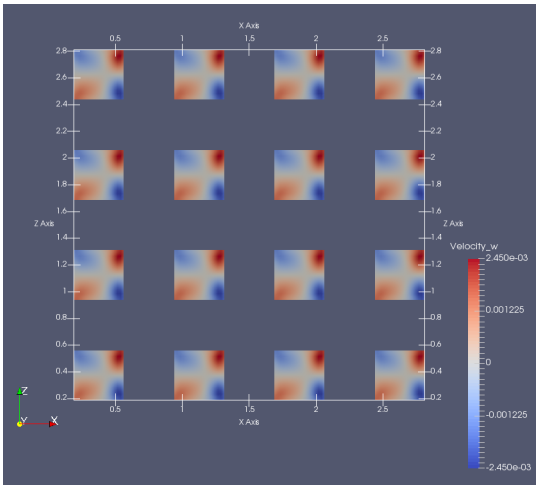

(b) $Re = 20000$

Figure 27: Spanwise velocity field on xz-slice at $y = 0$ inside the domain at $Re = 6000$ (a) and $Re = 20000$ (b)

The more pronounced 3D effects influence also the heat transfer inside the flow, thus the temperature field in the most affected region (i.e. nearby the pore intake), as can be seen in figure 28, which shows the temperature field on a xz-slice at $y = 0$. As can be seen, the higher temperature region at the pore surface is located near the right side for both cases, which the side in correspondence of the strong compression zone.

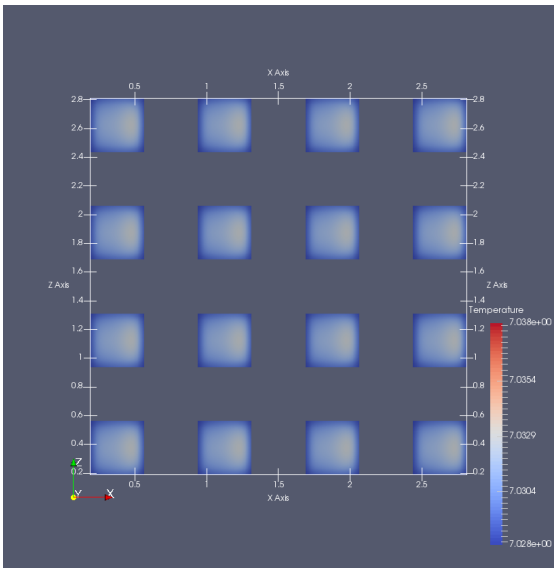

(a) $Re = 6000$

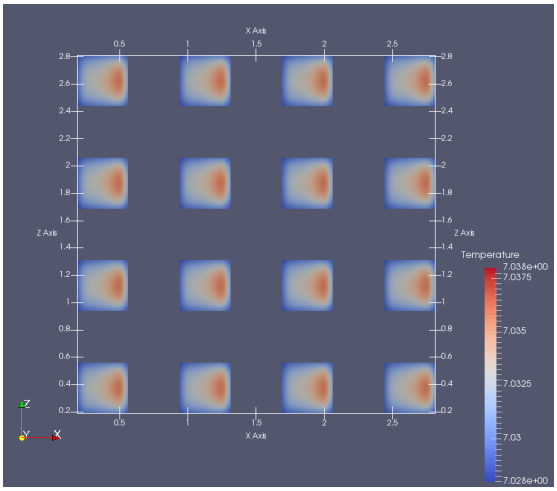

(b) $Re = 20000$

Figure 28: Temperature field on xz-slice at $y = 0$ inside the domain at $Re = 6000$ (a) and $Re = 20000$ (b)

However, in the higher Reynolds number case, the temperature reaches higher maximum values compared to the lower Reynolds number case. This is, again, in contrast to what observed in the 2D case (e.g. in figure 13), but consistent with the zone of maximum absolute value of the inwards velocity corresponding approximately to the flow region of higher temperatures, at the higher Reynolds number (as seen in figure 26). In fact, the higher inwards flow

in this region suggests that more hot fluid is taken from the near-wall boundary layer (where the high temperature values are located) and conducted into the pores.

Hence, the 3D flow configuration has shown some important differences with respect to the 2D case, which reflect in different flow features between a low and a high Reynolds number case. These effects need to be further analysed, in conjunction with the effects relative, for example, to the insertion of disturbances inside the boundary layer, of cold-fluid injection from the pores, and of different structures of the porous surface, in order to describe in more details their role in the stabilisation properties of a porous coating for transpiration cooling applications.

7 Conclusion

Two-dimensional and three-dimensional DNS simulations have been carried out to study the flow features of a Mach 6 hypersonic flow at different Reynolds numbers over a porous flat plate with periodic holes.

Preliminary 2D simulations have been run to validate the code (AMROC) and its performances, showing a very good agreement with results obtained from another high-resolution DNS code (SBLI). In particular, the high-resolution hybrid WENO-CD method implemented in AMROC has shown to be the most efficient method for the considered problem.

Further 2D simulations have been permormed to obtain a first parametric study of the solution at different Reynolds numbers and isothermal wall temperature conditions. This parametric study has shown that at a lower Reynolds number higher pressure levels are reached inside the pores, and stronger acoustic waves are radiated from the pore corners. Also, higher absolute values of the vertical velocity are formed inside the pores for the lower Reynolds number case, thus indicating a higher capability of the pores to trap fluid from outside due to the viscosity effects. Wall cooling, instead, has been shown to cause a thinner and distorted boundary layer, and the generation of stronger acoustic waves.

The 3D cases have shown the high-resolution DNS capabilities of the code, showing high-quality solutions and details of the main 3D flow characteristics. A 6^{th}-order WENO-CD method has been used to carry out these simulations, which has been shown to provide highly accurate results in the high gradient regions and for the travelling acoustic wave field. The 3D simulations, which have been performed for two different Reynolds numbers, have confirmed the above mentioned effect of the Reynolds number on the radiated pressure waves. In particular, a further analysis of the rms pressure levels outside of the boundary layer has shown pressure disturbance levels of about 4.5% and 1.54% of the presssure value in the unperturbed flow for the low and the high Reynolds number cases respectively. The 3D results have also shown that a higher Reynolds

number flow is more affected by 3D effects localised at the pore intake. These 3D effects are due to a higher spanwise flow going out of the pores, which, in turn, induces hot-fluid from the near-wall boundary layer to enter the pores, thus enhancing (in contrast with the 2D case) flow recirculation within the pores, and an increase of the maximum temperature reached on the pore intake surface.

This work has confirmed the DNS capabilities of our code to resolve a 3D hypersonic laminar flow over a porous coating, providing a first important assessment of the main 3D flow characteristics for the considered configuration. Hence, it represents a basis for a future investigation of the effectiveness and optimisation of next-generation transpiration cooling systems with hypersonic boundary-layer stabilisation capabilities.

References

[1] Anderson, J. D. *Hypersonic and High Temperature Gas Dynamics*, AIAA Education Series, 2000

[2] Fedorov, A. V., Malmuth, N. D., Rasheed, A., and Hornung, H. G., *Stabilization of hypersonic boundary layers by porous coatings*, AIAA Journal, 39(4), pp. 605-610, 2001

[3] Mack, L. M. *Boundary-layer linear stability theory*, Tech. Rep. ADP004046, California Inst. of Technology, Pasadena JPL, 1984

[4] Stetson, K. F., Thompson, E. R., Donaldson, J. C., and Siler, L. G. *Laminar boundary layer stability experiments on a cone at Mach 8. ii- blunt cone*, AIAA Aerospace Sciences Meeting 22nd, Reno, Nevada, 1984

[5] Fedorov, A. V., and Khokhlov, A. P. *Prehistory of Instability in a Hypersonic Boundary Layer*, Theoretical and Computational Fluid Dynamics 14 (6), 2001

[6] Fedorov, A. V. *Transition and Stability of High-Speed Boundary Layers*, Annual Review of Fluid Mechanics 43 (1), 2011

[7] Ma, Y., and Zhong, X. *Receptivity of a supersonic boundary layer over a flat plate, Part 3: Effects of different types of free-stream disturbances*, Journal of Fluid Mechanics 532, 2005

[8] Kara, K., Balakumar, P., and Kandil, O. A. *Receptivity of Hypersonic Boundary Layers Due to Acoustic Disturbances over Blunt Cone*, AIAA Pap. 945, 2007

[9] Malik, M. R., and Balakumar, P. *Acoustic receptivity of Mach 4.5 boundary layer with leading-edge bluntness*, Theoretical and Computational Fluid Dynamics, 21 (5), 2007, pp. 323-342

[10] Egorov, I. V., Sudakov, V. G., and Fedorov, A. V. *Numerical modeling of the receptivity of a supersonic boundary layer to acoustic disturbances*, Fluid Dynamics 41 (1), 2006

[11] Fedorov, A., Shiplyuk, A., Maslov, A., Burov, E., and Malmuth, N., *Stabilization of a hypersonic boundary layer using an ultrasonically absorptive coating*, Journal of Fluid Mechanics, 479, pp. 99-124, 2003

[12] Fedorov, A. V., Kozlov, V. F., Shiplyuk, A. N., Maslov, A. A., and Malmuth, N. D., *Stability of hypersonic boundary layer on porous wall with regular microstructure*, AIAA journal, 44(8), pp. 1866-1871, 2006

[13] Lukashevich, S. V., Morozov, S. O., and Shiplyuk, A. N., *Experimental study of the effect of a passive porous coating on disturbances in a hypersonic boundary layer 2. Effect of the porous coating location*, Journal of Applied Mechanics and Technical Physics, 57(5), pp. 873-878, 2016

[14] Chokani, N., Bountin, D. A., Shiplyuk, A. N., and Maslov, A. A., *Nonlinear aspects of hypersonic boundary-layer stability on a porous surface*, AIAA journal, 43(1), pp. 149-155, 2005

[15] Wang, X., and Zhong, X. (2012), *The stabilization of a hypersonic boundary layer using local section*, Physics of fluids, 24(3), 2012

[16] Wartemann, V., Ldeke, H., and Sandham, N. D., *Numerical investigation of hypersonic boundary-layer stabilization by porous surfaces*, AIAA journal, 50(6), pp. 1281-1290, 2012

[17] Wartemann, V., Wagner, A., Kuhn, M., Eggers, T., and Hannemann, K., *Passive hypersonic boundary layer transition control using an ultrasonically absorptive coating with random microstructure: Computational analysis based on the ultrasonic absorption properties of carbon-carbon*, Procedia IUTAM, 14, pp. 413-422, 2015

[18] Lukashevich, S. V., Maslov, A. A., Shiplyuk, A. N., Fedorov, A. V., and Soudakov, V. G., *Stabilization of high-speed boundary layer using porous coatings of various thicknesses*, AIAA journal, 50(9), pp. 1897-1904, 2012

[19] Deiterding, R., *Construction and application of an AMR algorithm for distributed memory computers*, Adaptive Mesh Refinement Theory and Applications, Lecture Notes in Computational Science and Engineering, vol. 41, Springer, pp. 361372, 2005

[20] Deiterding, R., *Detonation structure simulation with AMROC*, High Performance Computing and Communications 2005, Lecture Notes in Computer Science, vol. 3726, Springer, pp. 916927, 2005

[21] Hill, D.J. , Pullin, D.I., *Hybrid tuned center-difference-WENO method for large eddy simulations in the presence of strong shocks*, Journal of Computational Physics, 194(2), pp. 435450, 2004

[22] Martn, M. P., Taylor, E. M., Wu, M., and Weirs, V. G., *A bandwidth-optimized WENO scheme for the effective direct numerical simulation of compressible turbulence*, Journal of Computational Physics, 220(1), pp. 270-289, 2006

[23] Ziegler, J. L., Deiterding, R., Shepherd, J. E., and Pullin, D. I., *An adaptive high-order hybrid scheme for compressive, viscous flows with detailed chemistry*, Journal of Computational Physics, 230(20), pp. 7598-7630, 2011

[24] Jiang, G. S., and Shu, C. W., *Efficient implementation of weighted ENO schemes. Journal of computational physics*, 126(1), pp. 202-228, 1996

[25] De Tullio, N., and Sandham, N. D., *Direct numerical simulation of breakdown to turbulence in a Mach 6 boundary layer over a porous surface.* Physics of Fluids, 22(9), 2010

[26] De Tullio, N., Paredes, P., Sandham, N. D., and Theofilis, V., *Laminar-turbulent transition induced by a discrete roughness element in a supersonic boundary layer*, Journal of Fluid Mechanics 735, pp. 613-646, 2013